Pronounced Surface Band Bending of Thin-Film Silicon Revealed by Modeling Core Levels Probed with Hard X-rays

David Wippler*§, Regan G. Wilks#⊥, Bart E. Pieters§, Sacha J. van Albada&, Dominic Gerlach#‡, Jürgen Hüpkes*§, Marcus Bär#⊥∥ and Uwe Rau§

§IEK-5 Photovoltaik and &Institute of Neuroscience and Medicine Computational and Systems Neuroscience & Institute for Advanced Simulation Theoretical Neuroscience & JARA BRAIN Institute I, Forschungszentrum Jülich GmbH, Wilhelm-Johnen-Straße, D-52425 Jülich, Germany

#Renewable Energy, Helmholtz-Zentrum Berlin für Materialien und Energie GmbH, Hahn-Meitner-Platz 1, D-14109 Berlin, Germany

⊥Energy Materials In-Situ Laboratory Berlin (EMIL), Helmholtz-Zentrum Berlin für Materialien und Energie GmbH, Albert-Einstein-Str. 15, D-12489 Berlin, Germany

‡MANA/Nano-Electronics Materials Unit, National Institute for Materials Science (NIMS), 1-1 Namiki, Tsukuba, Ibaraki 305-0044, Japan

∥Institut für Physik und Chemie, Brandenburgische TU Cottbus, Konrad-Wachsmann-Allee 1, D-03046 Cottbus, Germany

1

ABSTRACT. Enhancing the probing depth of photoemission studies by using hard X-rays allows the investigation of buried interfaces of *real-world* device structures. However, it also requires the consideration of photoelectron-signal attenuation when evaluating surface effects. Here, we employ a computational model incorporating surface band bending and exponential photoelectron-signal attenuation to model depth-dependent spectral changes of Si 1s and Si 2s core level lines. The data were acquired from hydrogenated boron-doped microcrystalline thin-film silicon, which is applied in silicon-based solar cells. The core level spectra, measured by hard X-ray photoelectron spectroscopy using different excitation energies, reveal the presence of a 0.29 nm thick surface oxide layer. In the silicon film a downward surface band bending of $eV_{bb} = -0.65$ eV over approximately 6 nm obtained via inverse modeling explains the observed core level shifts and line broadening. Moreover, the computational model allows the extraction of the "real" Si 1s and Si 2s bulk core level binding energies as 1839.13 eV and 150.39 eV, and their natural Lorentzian line widths as 496 meV and 859 meV, respectively. These values significantly differ from those directly extracted from the measured spectra. Due to the fact that band bending usually occurs at material surfaces we highly recommend the detailed consideration of signal integration over depth for quantitative statements from depth-dependent measurements.

1. INTRODUCTION.

Band bending at surfaces and interfaces plays a crucial role for semiconductor (SC) device technologies.[1] Hence its characterization and understanding is of great importance. One of the most widely used methods to measure band bending is photoelectron spectroscopy (PES).[2–8] Hard X-ray PES (HAXPES) can achieve much larger information depths than common (soft X-ray and ultraviolet excited) PES methods and offers the unique possibility for depth-resolved PES-type characterization of band bending. [9–11] This is of particular interest for devices that rely on band bending such as field-effect transistors,[12–14] random access memories,[15,16] chemical sensors[17,18] and photochemical devices.[1] Band bending also occurs in heterojunction structures.

In silicon heterojunction (SHJ) solar cells, the operation relies on very thin doped alloyed silicon material on either side of the thus embedded wafer. Silicon heterojunction solar cells have recently achieved new record efficiencies for crystalline silicon devices.[19,20] The heterojunction usually consist of crystalline and hydrogenated, amorphous silicon (a-Si:H).[21] Transparent conductive oxides (TCO) serve as front contact. Due to its abundance, low material cost, and non-toxicity compared to other TCOs, zinc oxide (ZnO) is a reasonable front contact candidate material,[22,23] especially when doped with aluminum (ZnO:Al).[24,25] ZnO:Al can be easily prepared on large scale by sputtering[26] and has been successfully implemented in thin-film silicon photovoltaic technologies for several years.[27,28] Studies on p-i-n a-Si:H solar cells have shown that a hydrogenated microcrystalline and boron-doped (p-type) silicon (μc-Si:H:B) thin interlayer at the ZnO:Al/Si interface improves the device performance.[28–30] This finding also proved to be relevant for SHJ cells.[31] In a previous publication, we reported an electronic level alignment at the μc-Si:H:B/ZnO:Al interface that is beneficial for tunnel junction formation, in

particular when compared to the hydrogenated amorphous silicon oxide alloy a-SiO$_x$:H:B/ZnO:Al electronic interface.[32]
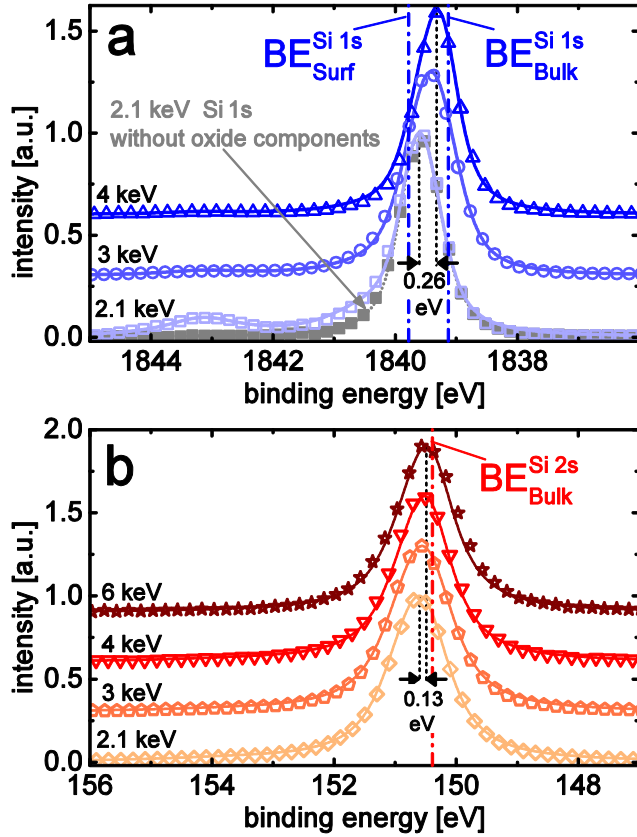

Figure 1. Measured Si 1s (a) and Si 2s (b) core level (CL) lines (symbols, every second data point is shown) of μc-Si:H:B excited with different excitation energies $h\upsilon$. A linear background is subtracted and vertical offsets are added for clarity. The solid lines depict the sum of the fitted Si^{1+} and Si^{4+} (see Figure 2) and the Si-Si model best fit for an ASA[35]-generated band bending (parameter values in Table 1, associated band bending in Figure 3). In addition, we present the 2.1 keV Si 1s data with subtracted oxygen contribution (grey filled squares) and the corresponding modeled CL line (grey dotted line) for comparison. The measured CL shifts and the model-derived CL positions for bulk (BE$_{Bulk}$) and surface (BE$_{Surf}$, only for the Si 1s spectra) are indicated by vertical lines.

In that HAXPES study on a 38.5 nm thick μc-Si:H:B layer deposited on a ZnO:Al/glass substrate, the information depth was varied by measuring the Si 1s and Si 2s core levels (CL) at different excitation energies.[32,33] The measurements revealed the existence of a Si-O$_x$ contribution that decreases rapidly with increasing information depth, indicating surface oxidation. Moreover, we observed depth-dependent shifts of the Si-Si feature in the Si 1s and Si 2s CL spectra (see also Figure 1). The shifts are more pronounced for low kinetic energy (= excitation energy - binding energy) of the probed photoelectrons. As the HAXPES information depth (governed by the inelastic mean free path, IMFP, of the photoelectrons) increases with kinetic energy, such peak shifts are commonly explained by a pronounced surface band bending.[33,34]

The latter usually occurs due to intrinsic or extrinsic surface states and can be influenced by the spectroscopic method itself, if certain contacting schemes are used.[36] The related depletion region can reach several nm, especially for SCs with their low capacity for charge balancing. Unfortunately, the HAXPES measured total CL signal S_t is modified by the band bending itself, because it arises from an integration of depth-resolved CL signals S_z that are subject to photoelectron-signal attenuation. This affects energy position and shape of S_t: The observed energy shifts will be smaller than the actual band bending at the surface eV_{bb}, the bulk CL binding energy BE_{Bulk} will be over- or underestimated depending on the direction of band bending (down- or upward, respectively), and the measured CL line with its Lorentzian full width at half maximum $fwhm_{\Gamma\,St}$ will be broadened by the overlap of the depth-resolved CL signals S_z with their natural Lorentzian line width (i.e., the CL lifetime broadening) $fwhm_\Gamma$. We consider the convolution of attenuated, depth-dependent signals (CADDS) to accurately describe those related effects.

In this contribution, we use HAXPES data to investigate the oxidized surface layer and quantify the surface band bending by iteratively solving the inverse problem, i.e., fitting modeled HAXPES data to the experiments. The HAXPES model reproduces energy position and shape of CL lines according to a given band bending and IMFP while taking CADDS into account. The surface band bending was either calculated based on the depletion approximation (DA), which is often used for high quality crystalline semiconductors, or by ASA (Advanced Semiconductor Analysis)[35] incorporating the specific nature of defects in μc-Si:H:B. For the iterative solving of the inverse problem we applied an advanced minimization routine.

As a result, this allows us to extract the band bending profile, the Si 1s and Si 2s bulk CL binding energies and their natural Lorentzian line widths from the measured HAXPES data.

2. MATERIALS AND METHODS.

2.1. Sample preparation. The preparation of the investigated hydrogenated boron-doped (p-type) microcrystalline thin-film silicon (μc-Si:H:B) is described in detail elsewhere.[32,33] Briefly, μc-Si:H:B was deposited by plasma-enhanced chemical vapor deposition on a Corning Eagle XG glass substrate covered with a 650 nm thick sputtered aluminum-doped zinc oxide (ZnO:Al) layer. The deposition time was 400 s, resulting in a 38.5 nm thick μc-Si:H:B layer.[33] The sample was transferred from the deposition tool in Jülich to the analysis tool in Berlin in an evacuated vacuum container. Nevertheless, during packing and sample mounting, the sample was briefly exposed to ambient air.

2.2. Measurement details. Si 1s and Si 2s CL line HAXPES measurements of the μc-Si:H:B/ZnO:Al/glass sample were performed under grazing incidence excitation and at normal emission geometry using the HiKE endstation,[37] installed at the KMC-1 beamline[38] of the BESSY II synchrotron radiation facility, Berlin (Germany) with excitation energies $h\nu \in \{2.1, 3, 4, 6\}$ keV. The corresponding IMFPs for Si 1s and Si 2s photoelectrons in silicon or silicon oxides, respectively, were calculated using the Quases-Tougaard code.[39,40] For energy calibration Au 4f reference spectra of a clean Au foil were periodically measured, fitted and the Au 4f$_{7/2}$ positions set to a binding energy of 84.00 eV. The sample surface has been contacted and shortened to the substrate during the HAXPES measurement, to avoid the impact of X-ray irradiation on the band bending.

2.3. Computational details. The algorithm used to fit the experimental data is based on a computational model that considers CADDS. It offers a numerical solution of the following equation:

$$S_t(E) = \int_0^D e^{-\frac{z}{IMFP}} \cdot S_z(E - B(z))\, \mathrm{d}z \tag{1}$$

where S_t defines the measured thus total peak signal as the integration of CL signals S_z from atoms at position z below the surface of the specimen with thickness D. Each S_z is modified by the band profile $B(z)$ and multiplied with the depth-dependent exponential attenuation. Note that Equation 1 can also be written in the form of a convolution integral using the inverse function of the band profile. The depth-resolved CL lines S_z were represented by a Voigt profile for each Si 1s and Si 2s CL line, for which the Gaussian contribution was taken individually from the corresponding Au reference measurement for each excitation energy. To solve the inverse problem of fitting modeled CL lines to measured ones, a minimization routine based on a genetic algorithm was applied. More information is provided in the Supporting Information.
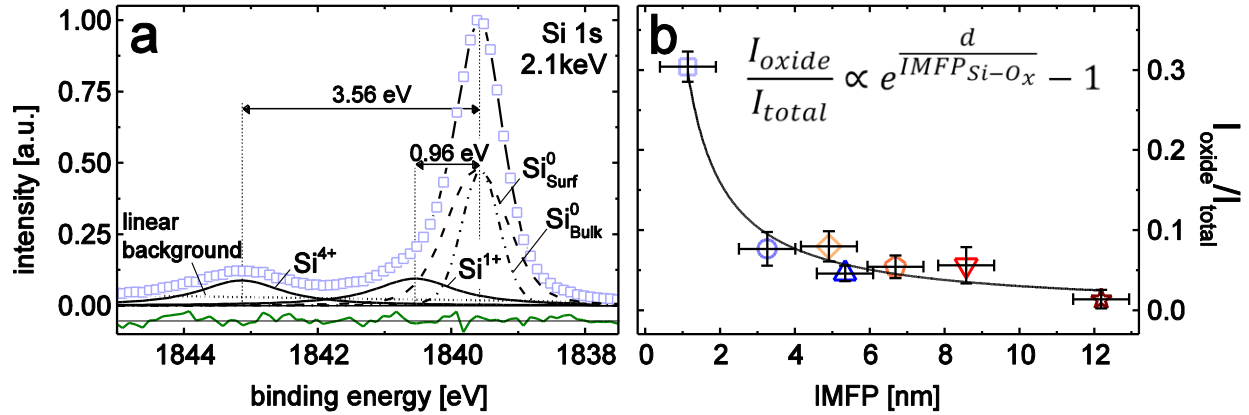
3. RESULTS AND DISCUSSION.

Figure 2. (a) Component fit of the 2.1 keV Si 1s CL spectrum of Figure 1. The different components related to Si-O$_x$ (Si^{4+} and Si^{1+}) and Si-Si bonds (Si$^0_{Surf}$ and Si$^0_{Bulk}$) as well as a linear background are shown. The fit residual (multiplied by a factor 3) is indicated at the bottom. Similar fits for all measured spectra allow the determination of the silicon oxide contribution. (b) By using an attenuation-based fit of the intensity ratio I_{oxide}/I_{total} (symbol shape/color code see Figure 1) and the assumption of the presence of a very thin homogeneous oxide layer located at the surface of the probed sample an oxide layer thickness of $d = (0.29 \pm 0.14)$ nm was derived.

3.1. Analysis of Surface Oxidation. The measured Si 1s and Si 2s CL spectra for different excitation energies are given in Figure 1a and b (symbols). Each spectrum consists of several signal components that are particularly prominent in the case of 2.1 keV Si 1s, representatively shown in Figure 2a. For the evaluation of the different contributions a regular curve-fitting procedure was used. We applied two Voigt profiles labeled as Si$^0_{Surf}$ and Si$^0_{Bulk}$ for the main Si-Si feature to account for the band bending induced asymmetry, one Voigt profile for each of the two obvious high-binding Si-O$_x$ signals, and a linear background. Note that Si$^0_{Surf}$ and Si$^0_{Bulk}$ do not represent the real surface and bulk signal but their area ratio equals the intensity ratio of all

9

signals from depth $z <$ IMFP (Si_{Surf}^0) to all signals from depth $z >$ IMFP (Si_{Bulk}^0). The peak shape of the Si-O$_x$ signal that forms the Si-Si peak shoulder at (1840.5 ± 0.1) eV was taken from the quite well defined Si-O$_x$ peak at (1843.14 ± 0.05) eV. From their energetic distance of about 2.6 eV we confirm these peaks to be attributable to the Si^{1+} and Si^{4+} chemical environment of Si surface oxides.[41–44] The larger error bar for the energetic position of the Si^{1+} peak is due to the larger fit uncertainty caused by the close proximity of the dominating Si-Si contribution (see also Figure S2 in Supporting Information).

With increasing excitation energy the Si^{1+} and Si^{4+} contributions to the total signal decrease rapidly (see Figure 2b and spectra in Figure 1). No significant asymmetry of their spectral shape or shift of their energetic positions is visible (see Figure S1a in the Supporting Information). This supports the assumption that the oxide signal stems from the very surface of the sample and thus is hardly affected by CADDS. The possibly different bond angle and length distribution for the Si-Si and Si-O$_x$ bonds in the silicon substrate and the surface oxide layer will affect the actual line shape and width, justifying the application of different Voigt profile widths describing the Si-Si and the Si-O$_x$ contributions in the fit (see Figure 2a and S2 in the Supporting Information).

We observe a shift of the Si-O$_x$ (Si^{4+}) relative to the Si-Si contribution of about $(0.5 - 0.7)$ eV – depending on the selected excitation energy – when comparing the Si 1s and Si 2s spectra. A similar shift is also reported in literature for surface oxidation on crystalline silicon as well as SiC,[45,46] and is explained by the different atomic charge state of the Si substrate and the Si-O$_x$ surface layer.[47] This shift can only be resolved for the Si^{4+} contribution, because the small Si^{1+} signal that forms the distinct Si-Si shoulder in the Si 1s spectra, is even more superposed by the broader Si-Si peak in the Si 2s spectra (see Figure S1b in the Supporting Information). Nevertheless, we applied the energetic distance of 2.6 eV between Si^{4+} and Si^{1+} as derived from

the Si 1s spectra also to fit the Si 2s spectra. Here we assume a homogeneous distribution of both Si-O$_x$ signals originating from the very thin surface oxide layer, so that their peak positions should be equally influenced by the charging effect.[47] Due to the low signal intensity of the Si 2s Si-O$_x$ (Si^{1+}) signal relative to the total signal (<5%) its impact on the following model fit is negligible as indicated by various calculations made with different signal component fit assumptions (not shown).

Figure 2b shows the oxide contribution intensity profile (i.e., the intensity ratio of the sum of Si^{4+} and Si^{1+} sub-oxides I_{oxide} and the total intensity I_{total} of the Si 1s and Si 2s spectrum) as function of IMFP calculated for Si 1s and Si 2s photoelectrons in Si-O$_x$, using the Quases-Tougaard code.[39,40] An attenuation-based fit of the intensity profile with the oxide thickness d as the only fit parameter is given by[48]

$$\frac{I_{\text{oxide}}}{I_{\text{total}}} \propto e^{\frac{d}{\text{IMFP}_{\text{Si}-\text{O}_x}}} - 1 \qquad (2)$$

(see also Figure 2b) and reveals the effective thickness of the surface oxide layer to be (0.29 ± 0.14) nm. Note that for this approach, it is assumed that the Si-O$_x$ contributions exclusively come from a homogeneous surface layer that completely covers the (O-free) μc-Si:H:B layer. The good fit of the data by this model (see Figure 2b) legitimizes this assumption.

The surface contamination of our samples is mainly attributed to the exposure to ambient air (at room temperature (RT)) during the transfer from deposition to the analysis tool. Thus, our findings fit well with studies on low exposure of molecular oxygen to Si surfaces,[49,50] initial layer-by-layer oxidation models,[51,52] and calculations of a barrierless oxidation of the uppermost Si layer.[52,53]

11

Further oxidation states, namely Si^{2+} and Si^{3+}, could not be resolved in our measurements in agreement with other studies on oxidized μc-Si:H.[54] This might be explained by the presence of carbon; in an oxidation study of SiC the absence of Si^{2+} and Si^{3+} surface oxidation states have also been reported[46] and indeed, surface carbon contamination was detected for our analyzed film with a C/Si surface ratio of $(21 \pm 5)\%$.[33]

The determination of the "true" bulk CL binding energies of Si 1s and Si 2s by the computational model – as described in detail in Section 3.2. – provides the possibility to examine the chemical shift of the $Si-O_x$ contributions, which is usually related to the energetic position of the CL Si-Si contribution as a function of IMFP. For the 2.1 keV Si 1s data with an IMFP of ~0.90 nm, relative shifts of (-0.96 ± 0.10) eV and (-3.56 ± 0.05) eV are measured for the $Si-O_x$ Si^{1+} and Si^{4+} contributions, respectively, as indicated in Figure 2a. These values agree well with Si 2p BE shifts reported in literature.[41–44] However, the respective BE shifts for the Si 1s line should be larger[45] due to the impact of net atomic charge.[47] When considering the model-derived bulk CL positions BE_{Bulk}, shown in Figure 1 as vertical dash-dotted lines (calculation details in Section 3.2.), the measured relative shifts translates into shifts of -1.41 eV and -4.01 eV for the Si^{1+} and Si^{4+} contributions regarding $BE_{Bulk}^{Si\ 1s}$ and -0.68 eV and -3.28 eV regarding $BE_{Bulk}^{Si\ 2s}$, respectively.[55] It also determines the atomic charge induced, relative shift between Si 1s and Si 2s to an absolute value of 0.73 eV (see Figure S1 in the Supporting Information).

More details on the curve-fitting procedure and the resulting fits for all CLs and excitation energies are available in the Supporting Information as well as a legitimization of our surface – bulk two-component fit of the Si-Si feature illustrated in Figure 2a.

3.2. Modeling of Core Level Lines. A description of the computational model can be found in Section 2.3. and more detailed information are provided in the Supporting Information. We here define the term 'model fit' for model-generated CL lines in order to avoid confusion with any curve-fitting procedure regularly used in PES for CL line fits (e.g., as employed for the determination of the Si-O$_x$ contribution in Section 3.1.). For this model fit, a linear background was removed from all measured spectra before the detailed analysis.

The band profile of the electronic band structure was generated by ASA (Advanced Semiconductor Analysis),[35] which is dedicated to the modeling of thin-film silicon materials like hydrogenated amorphous or microcrystalline silicon. ASA simulates the space-charge effects associated with the presence of partially occupied quasi-continuum density of states (DOS) within the band gap (band-tail states and dangling bonds).[56,57] As a result, ASA allows modeling the strong dependency of the space charge on the position of the Fermi level. Note that we do not attempt to describe the surface oxide and/or contaminated surface by ASA as it is difficult to obtain a meaningful parameterization. However, from the measured CL spectra the surface oxide contribution has been subtracted. For this reason we can effectively model the impact of surface-induced defect states with the band bending at the surface eV_{bb}. Although the focus will be on the ASA-generated band bending (unless otherwise stated), we also provide data on a first-order depletion approximation (DA). The DA model emulates the electrical properties of crystalline SCs without defect states in the band gap. Here, the surface charge that causes the band bending is compensated by ionized donors or acceptors in the space-charge region. Thus, a constant space-charge density is assumed in the depletion region of the width w_{dr} with an abrupt truncation for $z > w_{dr}$, leading to a DA-generated parabolic band bending near the surface. The depletion approximation works well for crystalline material with a tail-free band gap and a

constant doping concentration but is less suited for disordered semiconductor thin films. Nevertheless, we apply this more familiar approach to allow an appropriate comparison with a simple parabolic extrapolation of measured data.

Figure 1 shows the respective model fits (lines) in comparison to the measured data (symbols). After subtracting the high binding energy peaks attributed to Si-O_x bonds as discussed in Section 3.1., the inverse algorithm was applied simultaneously to all measured Si-Si core level contributions and excitation energies (represented in different colors). Note that only the upper 95% signal intensity of the measured data was considered for the model fit to avoid background effects. Once we obtained the model best fit, the surface Si-O_x components were added to the corresponding model-generated Si-Si CL lines which result in the solid lines in Figure 1. This allows a direct comparison to the measured spectra (open symbols). For clarity, we representatively inserted the pure modeled CL line (grey dotted line) and the corresponding measured CL line without the Si-O_x components (grey filled squares), for the 2.1 keV Si 1s spectrum in Figure 1a. In general, we obtain a good agreement in the fitted regime between measured and modeled CL lines with respect to CL shifts, broadening, and asymmetry. The bulk CL binding energies for Si 1s ($BE_{Bulk}^{Si\,1s}$) and Si 2s ($BE_{Bulk}^{Si\,2s}$) and the binding energy at the surface for the surface sensitive Si 1s CL ($BE_{Surf}^{Si\,1s}$) as derived by the model fit are indicated by vertical dash-dotted lines.

Table 1 lists the parameter values of the ASA model best fit shown in Figure 1. The third column gives the parameter ranges that will produce a fit within 10% of the error associated with the model best fit (see Figure S3 in the Supporting Information). The bottom part of Table 1 lists the parameter values of the DA model best fit. The averaged root-mean-square deviation

(avg. RMSD) of the model best fit to measured data is also given, indicating a 10% larger averaged RMSD for the DA compared to the ASA model. More information on the averaged RMSD, model parameters, and their ranges can be found in the Supporting Information.

Table 1. Model best fit parameters

ASA-modeled band bending (avg. RMSD: 0.0492)		
eV_{bb} [eV]	-0.65	[-0.73, -0.57]
n_{db} [10^{20} cm^{-3}]	0.68	[0.07, 1.79]
$BE_{Bulk}^{Si\,1s}$ [eV]	1839.13	[1838.89, 1839.21]
$BE_{Bulk}^{Si\,2s}$ [eV]	150.39	[150.17, 150.43]
$fwhm_{\Gamma}^{Si\,1s}$ [meV]	496	[425, 567]
$fwhm_{\Gamma}^{Si\,2s}$ [meV]	859	[791, 927]
DA-modeled band bending (avg. RMSD: 0.0541)		
eV_{bb} [eV]	-0.53	[-0.64, -0.45]
w_{dr} [nm]	5.9	[3.6, 15.2]
$BE_{Bulk}^{Si\,1s}$ [eV]	1839.19	[1838.98, 1839.25]
$BE_{Bulk}^{Si\,2s}$ [eV]	150.43	[150.26, 150.46]
$fwhm_{\Gamma}^{Si\,1s}$ [meV]	519	[442, 596]
$fwhm_{\Gamma}^{Si\,2s}$ [meV]	865	[784, 946]

Best fit results of ASA-generated, modeled Si-Si CL lines to measured data (see Figure 1), followed by best fit results for the depletion approximation (DA) model and their averaged root-mean-square deviation (avg. RMSD, see Supporting Information); from left to right column: parameter names (band bending eV_{bb}, dangling bond defect density n_{db} (ASA) and depletion region width w_{dr} (DA), bulk CL binding energy BE_{Bulk}, natural Lorentzian line width $fwhm_{\Gamma}$), model best fit parameter values, and +10% error ranges. The associated depth-resolved band profiles/CL positions are given in Figure 3.

Figure 3a presents the measured CL peak maximum positions vs. IMFP (magenta filled symbols) and the depth-resolved band profile (magenta solid line) corresponding to the ASA model best fit parameters of Table 1 that results in the modeled CL lines in Figure 1. Furthermore, the measured CL peak maximum positions and the band profile according to the DA model are also shown (blue open-crossed symbols, blue dashed line).
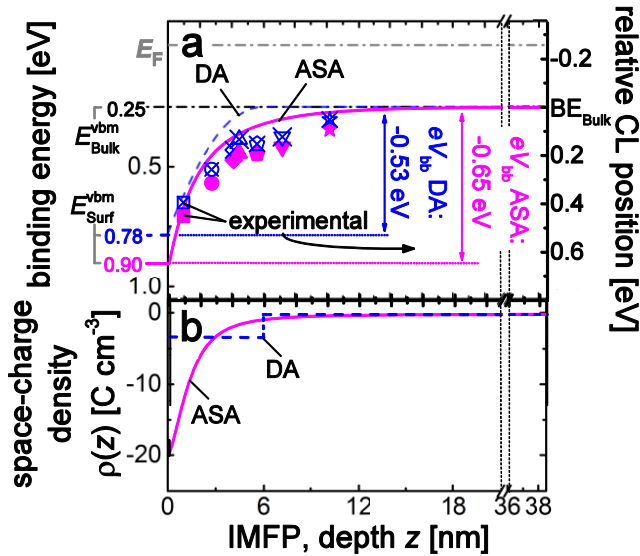

Figure 3. (a) Measured Si 1s and Si 2s CL maxima vs. corresponding IMFPs (symbols) and the associated depth-resolved band profile/CL position vs. depth z (lines) for the model best fit concerning ASA (magenta solid line, filled symbols) and the depletion approximation DA (blue dashed line, open-crossed symbols). The symbols represent Si 1s [Si 2s] with increasing excitation energies $h\nu \in \{2.1, 3, 4, [6]\}$ keV: square [diamond], circle [pentagon], upward-pointing [downward-pointing] triangle, [asterisk]; the left and right axes illustrate binding energy (valence band maximum, vbm) relative to E_F and CL position relative to the Si 1s or Si 2s bulk CL (BE_{Bulk}), respectively. The difference in model-calculated BE_{Bulk} between DA and ASA (see Table 1) explains the vertical offset of the same measured data. (b) Related space-charge density $\rho(z)$ for the ASA (magenta solid line) and the DA (blue dashed line) model.

16

The left energy scale refers to the position of the valence band maximum (vbm) of μc-Si:H:B relative to the Fermi level E_F. The position of the valence band maximum in the bulk (E_{Bulk}^{vbm}) of 0.25 eV was determined from the leading edge of the valence band recorded by HAXPES with an excitation energy of 3 keV.[32] For this estimation, we qualitatively took the influence of CADDS on the valence band spectrum into account. Calculations based on an independent dark conductivity measurement of similar p-doped μc-Si:H samples, deposited in the same process chamber, lead to values between 0.2 and 0.3 eV for E_{Bulk}^{vbm}.[58,59]

The right-hand energy scale is offset by the model-calculated bulk CL binding energy of Si 1s and Si 2s, respectively (see also vertical dash-dotted lines in Figure 1). In this respect, the magenta solid line (ASA) or blue dashed line (DA) depicts the depth-resolved position of the CL lines S_z with respect to their bulk binding energy BE_{Bulk}.[60,61] The measured CL peak maximum positions for different excitation energies (symbols; shape code see Figure 1) are displayed vs. their corresponding IMFP in Si.[39,40] The Si 1s and Si 2s CL maxima are aligned on the energy scale according to model best fit results for the respective BE_{Bulk} (see Table 1). Therefore their energetic difference to BE_{Bulk} (black dash-dotted line) equals the distance between the measured CL peak maximum positions and the vertical dash-dotted line in Figure 1a and b. The deviation of BE_{Bulk} between ASA and DA (see Table 1) results in the different alignment of the same measured CL peak maximum positions of Si 1s and Si 2s relative to BE_{Bulk} (ASA: magenta filled symbols, DA: blue open-crossed symbols) in Figure 3a.

Note that so far we have assumed flat-band conditions at the μc-Si:H:B/TCO interface. However, this assumption is probably not valid. For this reason we tested various interface band bending situations and found that for realistic scenarios and all used IMFPs the impact on the modeled

CADDS-related effects are negligible (not shown). Thus the surface band bending is not affected by the possibly existing band bending at the μc-Si:H:B/TCO interface. However, this might again be different for thinner silicon layers.

3.2.1. Surface Band Bending eV$_{bb}$. The ASA model-predicted band profile in Figure 3a (magenta solid line) shows a pronounced downward surface band bending of $eV_{bb} = (-0.65 \pm 0.08)$ eV over approximately 20 nm. Note that 90% of that band bending occurs within the topmost 6 nm. According to the ASA model this is caused by a high space-charge density $\rho(z)$ near the surface as illustrated in Figure 3b (magenta solid line). This charge compensates a positive surface-charge density of $3.47 \cdot 10^{-6}$ C cm^{-2}, which roughly corresponds to 0.02 electrons per surface atom.[62] The surface valence band maximum $E_{\mathrm{Surf}}^{\mathrm{vbm}}$ is determined to be 0.90 eV below E_F, since in the charge-neutral region (i.e., the sample bulk), $E_{\mathrm{Bulk}}^{\mathrm{vbm}}$ was estimated to be 0.25 eV below E_F.[32] Assuming a band gap at the surface close to that reported for the μc-Si:H:B bulk of 1.25 eV[63,64] this results in E_F being closer to the conduction band minimum than to the valence band maximum, indicating a conduction type inversion at the surface.

For the DA model the generated surface band bending results in $eV_{bb} = [-0.53 \,(-\,0.11/+\,0.08)]$ eV with a depletion region width of $w_{dr} = 5.9$ nm (Figure 3a, blue dashed line). The resulting space-charge density was obtained by solving the Poisson equation,[61] which leads (assuming the relative permittivity of Si, ε_r (Si), to be approximately 11.8)[61] to a constant space-charge density of $\rho(z \leq w_{dr}) = -3.18$ C cm^{-3} and $\rho(z > w_{dr}) = 0$ (Figure 3b, blue dashed line) and a related surface-charge density of $1.88 \cdot 10^{-6}$ C cm^{-2} (~0.01 electrons per surface atom).[62] Note that the space-charge density of μc-Si:H:B consists of both ionized acceptors as well as trapped electrons in dangling-bond and band-tail states.[56,57]

To demonstrate the effect of neglecting CADDS we also determined the surface band bending by solely considering the experimental data, i.e. we interpret the energy of a CL maximum as a direct measure of the CL position at a depth equal to the IMFP. This results in a value of $eV_{bb} = (-0.39 \pm 0.10)$ eV for the surface band bending obtained by the sum of the measured CL shifts for Si 1s and Si 2s. A more accurate value of $eV_{bb} = (-0.45 \pm 0.03)$ eV with a depletion region of about 9.9 nm is obtained using a parabolic extrapolation of the measured data to the surface (see also Supporting Information). Comparable values for eV_{bb} are reported in literature for PES studies on Si material with similar surface oxidation,[3] and boron doping concentration.[6,8] However, it is already mentioned in these reports that band bending may not be visible to its full extent due to the possible impact of CADDS on the measured CL shift. Indeed, even in comparison to the DA model which considers CADDS, the band bending derived solely by analyzing the measured CL shifts is underestimated. Additionally, the respective band profile steepness is quite different, which is mainly caused by the narrower depletion region of the DA model. Similarly to the DA model, the parabolic extrapolation does not describe the disorder of microcrystalline silicon, whose complex defect distribution cannot be integrated in a simple data fitting procedure. Some recent HAXPES studies of band bending already took photoelectron-signal attenuation combined with a case-dependent band profile into account.[9–11] For our μc-Si:H:B, the ASA-generated band profile is more accurate and with $eV_{bb} = (-0.65 \pm 0.08)$ eV significantly larger than the parabolic DA band profile with $eV_{bb} = [-0.53 (-0.11/+0.08)]$ eV. However, it is verified by surface-sensitive investigations on similar doped p-type Si with C- and O-impurities at the surface by Demuth et al., who reported a temperature-dependent valence band spectral shift of (-0.65 ± 0.02) eV that they attributed to surface band bending.[65] Note that this study is hardly affected by CADDS because it is based on He I (21.2 eV) and He II

(40.8 eV) excited (i.e., very surface sensitive) PES measurements of the valence band edge. Although the mentioned values from literature are related to crystalline silicon, our results show that the defect states at the surface apparently lead to a similar surface Fermi level position for μc-Si:H:B.

3.2.2. Bulk Core Level Binding Energy BE_{Bulk}. The binding energies of the CL lines in the bulk provided in Table 1 and indicated as vertical dash-dotted lines in Figure 1 lie at lower binding energies compared to the experimental CL line maxima. The peak shifts are more pronounced for lower photon energies, and for the more surface-sensitive Si 1s measurements. Figure 3a allows a good comparison between the energetic positions of BE_{Bulk} (black dash-dotted line) and modeled (solid line) and measured (filled symbols) CL positions for different depths or IMFPs. The deviation between the actual energetic position of electrons released at depth z and the measured peak positions with an IMFP of same value is especially prominent in the central range of the band bending ($\sim$ 3 - 8 nm). This discrepancy directly quantifies the impact of CADDS on the CL shift for a given depth or IMFP, respectively. The consequence is the inaccessibility of BE_{Bulk} directly from measured data in the presence of a pronounced surface band bending, though HAXPES measurements offer quite large IMFP. The model best fit reveals $BE_{Bulk}^{Si\ 1s}$ to be [1839.13 (- 0.24/+ 0.08)] eV and $BE_{Bulk}^{Si\ 2s}$ to be [150.39 (- 0.22/+ 0.04)] eV. The DA calculated bulk CL binding energies differ only slightly from those obtained from ASA (see Table 1). This insensitivity to the model assumptions demonstrates the reliability of this approach.

An interesting aspect of the model-calculated BE_{Bulk} values is the resulting offset between Si 1s and Si 2s CL maximum positions for equal IMFPs. The CL maxima with similar IMFP ($\sim$ 4 nm) in Figure 3a illustrate this point. It is explained by the different natural Lorentzian line width

(lifetime broadening) of the Si 1s and Si 2s CL line, which affects the impact of CADDS on the CL line shape and maximum position.

3.2.3. Natural Lorentzian Line Width $fwhm_\Gamma$. CADDS causes a broadening of the measured CL lines due to the energy shift within the region producing the integrated signal.[66] The line broadening and the degree of its asymmetry depend on the ratio of band bending to the natural CL line width and the ratio of depletion width to information depth. Thus, commonly the Lorentzian line width extracted from fits of the measured signals ($fwhm_{\Gamma\,St}{}^{*e}$) is overestimated.

In Table 2, the CL peak shape analysis is summarized. Each Gaussian contribution ($fwhm_\sigma{}^{*e}$) to the Voigt function was extracted from the Voigt fits of the Au $4f_{7/2}$ calibration measurements for each excitation energy, and was held constant in the computational model. The value of the natural Lorentzian line width $fwhm_\Gamma$ was determined by the model-procedure. Thus we find $fwhm_\Gamma$ to be (496 ± 71) meV and (859 ± 68) meV for the Si 1s and Si 2s CL, respectively (see also Table 1). They show, as already noticed for the bulk CL binding energies, a weak dependency on the chosen model (ASA or DA).

Any broadening attributable to disorder in the material will tend to increase $fwhm_\Gamma$, because the Gaussian contribution was attributed to the measurement setup. Nonetheless, our values are in agreement with predictions for the lifetime broadening.[67,68]

Table 2. CL peak shape analysis

CL	Si 1s			Si 2s			
$h\nu$ [keV]	2.1	3	4	2.1	3	4	6
IMFP [nm]	0.90	2.68	4.42	4.07	5.55	7.12	10.13
fwhm$_\sigma$ [meV] [*e]	364	511	312	364	458	312	367
fwhm$_\Gamma$ [meV]	496	496	496	859	859	859	859
fwhm$_{\Gamma\,St}$ [meV] [*m]	582	648	675	978	964	963	945
fwhm$_{\Gamma\,St}$ [meV] [*e]	576	642	608	939	904	968	984

    CL peak shape analysis of the model best fit for ASA: Listed are the type of core level CL, the excitation energy $h\nu$ and resulting IMFP,[39,40] the measured Gaussian fwhm$_\sigma$, and the modeled natural Lorentzian line width fwhm$_\Gamma$. The extracted Lorentzian fwhm$_{\Gamma\,St}$ is increased by CADDS and given for both modeled ([*m]) and measured ([*e]) CL lines.

The modeled total fwhm$_{\Gamma\,St}$[*m] (the Lorentzian line width of the modeled HAXPES line) first increases with increasing IMFP due to the very steep band bending profile close to the surface. For larger IMFP, the fraction of surface-related signal S_z and thus the peak width decrease. This trend is not observed in the experimental CL fwhm$_{\Gamma\,St}$[*e]. There are several possible explanations, and we speculate that in particular the strongly disordered surface plays a crucial role. First, although the ASA model incorporates band-tail states and dangling bonds, it is still an approximation of μc-Si:H:B, and thus may not include all occupied defect states, especially not those that are close to the surface of the investigated material. Therefore, the real band profile could still differ from our ASA-generated one, affecting how the depth-dependent CL lines are modified. Next, our calculated natural Lorentzian line widths for Si 1s and Si 2s are averaged over all depths z. However, we expect the real Lorentzian line widths of depth-resolved CL lines to slightly vary with depth, due to changes in the chemical environment according to the grain growth and thickness-dependent stress formation.[69] Finally, other physical or chemical mechanisms might be involved that are not accounted for in our model. This includes, for

instance, effects caused by the oxide layer at the surface. It is known that the $Si-O_x$ bonds, which are responsible for the chemical shift of the Si^{1+} and Si^{4+} signal, also slightly affect second following Si atoms in their vicinity,[42,70] which may result in the observable additional broadening of the surface-sensitive 2.1 keV and 3 keV Si 1s signals in Table 2.

4. CONCLUSIONS.

Employing a computational algorithm that considers surface band bending and photoelectron-signal attenuation, we modeled depth-dependent Si 1s and Si 2s CL lines measured for μc-Si:H:B films on a ZnO:Al coated glass substrate. The experimental observations were explained by a very thin surface oxide layer of (0.29 ± 0.14) nm and a significant downward band bending of (-0.65 ± 0.08) eV. The band bending extends from the surface over 20 nm into the silicon bulk with approximately 90% of the band bending occurring in the topmost 6 nm. By model fitting the data, we could extract the bulk CL binding energies of $[1839.13 \, (-0.24/+0.08)]$ eV and $[150.39 \, (-0.22/+0.04)]$ eV as well as their natural Lorentzian line widths of (496 ± 71) meV and (859 ± 68) meV for Si 1s and Si 2s, respectively. This also allows to estimate an offset for the Si-O$_x$ (Si^{1+} and Si^{4+}) contributions to the bulk CLs Si-Si contribution revealing absolute shifts for Si^{1+} and Si^{4+} of (-1.41 ± 0.10) eV and (-4.01 ± 0.05) eV for Si 1s, respectively, with an additional offset of (0.73 ± 0.10) eV to the bulk Si 2s Si-Si contribution. The consideration of the convolution of depth-dependent attenuated photoelectron-signals is important to extract those values from measurements with an appropriate accuracy. It requires the combination of both the experimental depth-dependent study and the analysis by a model that considers the specific properties of the investigated material. This applies in particular for the increasingly popular buried interface studies by HAXPES, for which band bending usually occurs at the surface and towards the buried interface of the investigated layer system.

ASSOCIATED CONTENT

Supporting Information. "Fit details for the quantification of the Si-O$_x$ and Si-Si contribution to the silicon core level lines, direct surface band bending calculation details, inverse modeling parameters and ranges, parameter error estimation. This material is available free of charge via the Internet at http://pubs.acs.org."

AUTHOR INFORMATION

Corresponding Author

*(E-mail: d.wippler@fz-juelich.de, Tel.:+49-2461-61-6310), *(j.huepkes@fz-juelich.de. Tel:+49-2461-61-2594).

Author Contributions

The manuscript was written through contributions of all authors. All authors have given approval to the final version of the manuscript.

Notes

The authors declare no competing financial interest.

REFERENCES

(1)   Zhang, Z.; Yates, J. T. Band Bending in Semiconductors: Chemical and Physical Consequences at Surfaces and Interfaces. *Chem. Rev.* **2012**, 112 (10), 5520–5551.

(2)   Himpsel, F.; Hollinger, G.; Pollak, R. Determination of the Fermi-Level Pinning Position at Si(111) Surfaces. *Phys. Rev. B* **1983**, 28 (12), 7014–7018.

(3)   Ranke, W.; Xing, Y. R. Surface Dipole and Fermi-Level Position on Clean, Oxygen-, and Water-Covered Cylindrical Si Crystals: A Photoelectron Spectroscopy Study. *Phys. Rev. B* **1985**, 31 (4), 2246–2253.

(4)   Jacobi, K.; Myler, U.; Althainz, P. Determination of Band Bending at the Si(113) Surface from Photovoltage-Induced Core-Level Shifts. *Phys. Rev. B* **1990**, 41 (15), 10721–10726.

(5)   Huang, L. J.; Lau, W. M. Surface Electrical Properties of HF-Treated Si(100). *J. Vac. Sci. Technol., A* **1992**, 10 (4), 812–816.

(6)   Schlaf, R.; Hinogami, R.; Fujitani, M.; Yae, S.; Nakato, Y. Fermi Level Pinning on HF Etched Silicon Surfaces Investigated by Photoelectron Spectroscopy. *J. Vac. Sci. Technol., A* **1999**, 17 (1), 164–169.

(7)   Long, J. P.; Bermudez, V. M. Band Bending and Photoemission-Induced Surface Photovoltages on Clean n- and p-GaN (0001) Surfaces. *Phys. Rev. B* **2002**, 66 (12), 121308-1– 121308-4.

(8)   Gleason-Rohrer, D. C.; Brunschwig, B. S.; Lewis, N. S. Measurement of the Band Bending and Surface Dipole at Chemically Functionalized Si(111)/Vacuum Interfaces. *J. Phys. Chem. C* **2013**, 117 (35), 18031–18042.

(9)   Tanaka, H.; Satoh, I.; Kanki, T.; Ikenaga, E.; Kobata, M.; Kim, J. J.; Ueda, S.; Kobayashi, K. Nondestructive Estimation of Depletion Layer Profile in Nb-Doped $SrTiO_3$/(La,Ba)MnO_3 Heterojunction Diode Structure by Hard X-Ray Photoemission Spectroscopy. *App. Phys. Lett.* **2011**, 98 (13), 133505-1–133505-3.

(10)   Minohara, M.; Horiba, K.; Kumigashira, H.; Ikenaga, E.; Oshima, M. Depth Profiling the Potential in Perovskite Oxide Heterojunctions Using Photoemission Spectroscopy. *Phys. Rev. B* **2012**, 85 (16), 165108-1–165108-6.

(11)   Minohara, M.; Hikita, Y.; Bell, C.; Inoue, H.; Hosoda, M.; Sato, H. K.; Kumigashira, H.; Oshima, M.; Ikenaga, E.; Hwang, H. Y. The Potential Profile at the $LaAlO_3$/$SrTiO_3$ (001) Heterointerface in Operando Conditions. *arXiv preprint arXiv:1403.5594* **2014**, 1–16.

(12)   Tucker, J. R.; Wang, C.; Carney, P. S. Silicon Field-Effect Transistor Based on Quantum Tunneling. *App. Phys. Lett.* **1994**, 65 (5), 618–620.

(13) Novoselov, K. S.; Geim, A. K.; Morozov, S. V.; Jiang, D.; Zhang, Y.; Dubonos, S. V.; Grigorieva, I. V.; Firsov, A. A. Electric Field Effect in Atomically Thin Carbon Films. *Science* **2004**, 306 (5696), 666–669.

(14) Xiang, J.; Lu, W.; Hu, Y.; Wu, Y.; Yan, H.; Lieber, C. M. Ge/Si Nanowire Heterostructures as High-Performance Field-Effect Transistors. *Nature* **2006**, 441, 489–493.

(15) Borgatti, F.; Park, C.; Herpers, A.; Offi, F.; Egoavil, R.; Yamashita, Y.; Yang, A.; Kobata, M.; Kobayashi, K.; Verbeeck, J.; Panaccione, G.; Dittmann, R. Chemical Insight into Electroforming of Resistive Switching Manganite Heterostructures. *Nanoscale* **2013**, 5 (9), 3954–3960.

(16) Lenser, C.; Köhl, A.; Patt, M.; Schneider, C. M.; Waser, R.; Dittmann, R. Band Alignment at Memristive Metal-Oxide Interfaces Investigated by Hard X-Ray Photoemission Spectroscopy. *Phys. Rev. B* **2014**, 90 (11), 115312-1–115312-8.

(17) Barsan, N.; Weimar, U. Conduction Model of Metal Oxide Gas Sensors. *J. Electroceram.* **2001**, 7 (3), 143–167.

(18) Patsha, A.; Sahoo, P.; Amirthapandian, S.; Prasad, A. K.; Das, A.; Tyagi, A. K.; Cotta, M. A.; Dhara, S. Localized Charge Transfer Process and Surface Band Bending in Methane Sensing by GaN Nanowires. *J. Phys. Chem. C* **2015**, 119 (36), 21251–21260.

(19) De Wolf, S.; Descoeudres, A.; Holman, Z. C.; Ballif, C. High-Efficiency Silicon Heterojunction Solar Cells: A Review. *Green* **2012**, 2 (1), 7–24.

(20) Ding, K.; Aeberhard, U.; Smirnov, V.; Holländer, B.; Finger, F.; Rau, U. Wide Gap Microcrystalline Silicon Oxide Emitter for a-SiO$_x$:H/c-Si Heterojunction Solar Cells. *Jpn. J. Appl. Phys.* **2013**, 52 (12R), 122304-1–122304-5.

(21) Rech, B.; Wagner, H. Potential of Amorphous Silicon for Solar Cells. *App. Phys. A: Mater. Sci. Process.* **1999**, 69 (2), 155–167.

(22) Ellmer, K.; Klein, A.; Rech, B. Transparent Conductive Zinc Oxide: Basics and Applications in Thin Film Solar Cells. *Springer Ser. Mater. Sci.* **2007**, 104.

(23) Beyer, W.; Hüpkes, J.; Stiebig, H. Transparent Conducting Oxide Films for Thin Film Silicon Photovoltaics. *Thin Solid Films* **2007**, 516 (2-4), 147–154.

(24) Kluth, O.; Rech, B.; Houben, L.; Wieder, S.; Schöpe, G.; Beneking, C.; Wagner, H.; Löffl, A.; Schock, H. Texture Etched ZnO:Al Coated Glass Substrates for Silicon Based Thin Film Solar Cells. *Thin Solid Films* **1999**, 351 (1-2), 247–253.

(25) Becker, C.; Conrad, E.; Dogan, P.; Fenske, F.; Gorka, B.; Hänel, T.; Lee, K. Y.; Rau, B.; Ruske, F.; Weber, T.; Berginski, M.; Hüpkes, J.; Gall, S.; Rech, B. Solid-Phase Crystallization of Amorphous Silicon on ZnO:Al for Thin-Film Solar Cells. *Sol. Energy Mater. Sol. Cells* **2009**, 93 (6-7), 855–858.

(26) Klein, S.; Wieder, S.; Buschbaum, S.; Schwanitz, K.; Stolley, T.; Severin, D.; Obermeyer, P.; Kress, M.; Sommer, E.; Marschner, T.; Martini, M.; Noll-Baumann, S.; Haack, J.; Schmidt, U. I.; Straub, A.; Ahmed, K.; Schuegraf, K. Large Area Thin Film Silicon Modules with 10% Efficiency for Mass Production. *Phys. Status Solidi C* **2011**, 8 (10), 2978–2981.

(27) Benagli, S.; Borrelo, D.; Vallat-Sauvain, E.; Meier, J.; Kroll, U.; Hoetzel, J.; Bailat, J.; Steinhauser, J.; Marmelo, M.; Monteduro, G.; Castens, L. High-Efficiency Amorphous Silicon Devices on LPCVD-ZNO TCO Prepared in Industrial Kai[TM]-M R&D Reactor. *Proceedings of the 24th European Photovoltaic Solar Energy Conference, Hamburg, Germany* **2009**, 2293–2298.

(28) Müller, J.; Kluth, O.; Wieder, S.; Siekmann, H.; Schöpe, G.; Reetz, W.; Vetterl, O.; Lundszien, D.; Lambertz, A.; Finger, F.; Rech, B.; Wagner, H. Development of Highly Efficient Thin Film Silicon Solar Cells on Texture-Etched Zinc Oxide-Coated Glass Substrates. *Sol. Energy Mater. Sol. Cells* **2001**, 66 (1-4), 275–281.

(29) Ma, W.; Aoyama, S.; Okamoto, H.; Hamakawa, Y. A Study of Interface Properties in a-Si Solar Cells with μc-Si(C). *Sol. Energy Mater. Sol. Cells* **1996**, 41/42, 453–463.

(30) Lee, J. C.; Dutta, V.; Yoo, J.; Yi, J.; Song, J.; Yoon, K. H. Superstrate P-I-N a-Si:H Solar Cells on Textured ZnO:Al Front Transparent Conduction Oxide. *Superlattices Microstruct.* **2007**, 42 (1-6), 369–374.

(31) Madani Ghahfarokhi, O.; Chakanga, K.; Geissendoerfer, S.; Sergeev, O.; von Maydell, K.; Agert, C. DC-Sputtered ZnO:Al as Transparent Conductive Oxide for Silicon Heterojunction Solar Cells with μc-Si:H Emitter. *Prog. Photovoltaics* **2014**, 23 (10), 1340–1352.

(32) Gerlach, D.; Wilks, R. G.; Wippler, D.; Wimmer, M.; Lozac'h, M.; Félix, R.; Mück, A.; Meier, M.; Ueda, S.; Yoshikawa, H.; Gorgoi, M.; Lips, K.; Rech, B.; Sumiya, M.; Hüpkes, J.; Kobayashi, K.; Bär, M. The Silicon/Zinc Oxide Interface in Amorphous Silicon-Based Thin-Film Solar Cells: Understanding an Empirically Optimized Contact. *Appl. Phys. Lett.* **2013**, 103 (2), 023903-1–023903-5.

(33) Gerlach, D.; Wippler, D.; Wilks, R. G.; Wimmer, M.; Lozac´h, M.; Félix, R.; Ueda, S.; Yoshikawa, H.; Lips, K.; Rech, B.; Sumiya, M.; Kobayashi, K.; Gorgoi, M.; Hüpkes, J.; Bär, M. P-Type a-Si:H/ZnO:Al and μc-Si:H/ZnO:Al Thin-Film Solar Cell Structures — A Comparative Hard X-Ray Photoelectron Spectroscopy Study. *IEEE Photovoltaic Spec. Conf. , 38th* **2013**, 2, 1–5.

(34) Skorupska, K.; Lublow, M.; Kanis, M.; Jungblut, H.; Lewerenz, H. J. Electrochemical Preparation of a Stable Accumulation Layer on Si: A Synchrotron Radiation Photoelectron Spectroscopy Study. *Appl. Phys. Lett.* **2005**, 87 (26), 262101-1–262101-3.

(35) ASA. ASA, Advanced Semiconductor Analysis, Version 5.30 degrading since 2012 (compiled on Feb 4 2013), © 1993/2013 Lab of ECIM / DIMES Delft University of Technology.

(36) Iwata, S.; Ishizaka, A. Electron Spectroscopic Analysis of the SiO2/Si System and Correlation with Metal–Oxide–Semiconductor Device Characteristics. *J. Appl. Phys.* **1996**, 79 (9), 6653–6713.

(37) Gorgoi, M.; Svensson, S.; Schäfers, F.; Öhrwall, G.; Mertin, M.; Bressler, P.; Karis, O.; Siegbahn, H.; Sandell, A.; Rensmo, H.; Doherty, W.; Jung, C.; Braun, W.; Eberhardt, W. The High Kinetic Energy Photoelectron Spectroscopy Facility at BESSY Progress and First Results. *Nucl. Instrum. Mehtods Phys. Res., Sect. A* **2009**, 601 (1-2), 48–53.

(38) Schaefers, F.; Mertin, M.; Gorgoi, M. KMC-1: A High Resolution and High Flux Soft X-Ray Beamline at BESSY. *Rev. Sci. Instrum.* **2007**, 78 (12), 123102-1–123102-14.

(39) QUASES. QUASES; http://www.quases.com/products/quases-imfp-tpp2m/.

(40) Tanuma, S.; Powell, C. J.; Penn, D. R. Calculations of Electron Inelastic Mean Free Paths. IX. Data for 41 Elemental Solids over the 50 eV to 30 keV Range. *Surf. Interface Anal.* **2011**, 43 (3), 689–713.

(41) Hollinger, G.; Himpsel, F. J. Multiple-Bonding Configurations for Oxygen on Silicon Surfaces. *Phys. Rev. B* **1983**, 28 (6), 3651–3653.

(42) Pasquarello, A.; Hybertsen, M. S.; Car, R. First-Principles Study of Si 2p Core-Level Shifts at Water and Hydrogen Covered Si(001)2×1 Surfaces. *J. Vac. Sci. Technol., B: Microelectron. Nanometer Struct.--Process., Meas., Phenom.* **1996**, 14 (4), 2809–2811.

(43) Yeom, H.; Hamamatsu, H.; Ohta, T.; Uhrberg, R. I. G. High-Resolution Core-Level Study of Initial Oxygen Adsorption on Si(001): Surface Stoichiometry and Anomalous Si 2p Core-Level Shifts. *Phys. Rev. B* **1999**, 59 (16), R10413–R10416.

(44) Jolly, F.; Rochet, F.; Dufour, G.; Grupp, C.; Taleb-Ibrahimi, A. Oxidized Silicon Surfaces Studied by High Resolution Si 2p Core-Level Photoelectron Spectroscopy Using Synchrotron Radiation. *J. Non-Cryst. Solids* **2001**, 280 (1-3), 150–155.

(45) Eickhoff, Th.; Medicherla, V.; Drube, W. Final State Contribution to the Si 2p Binding Energy Shift in SiO_2/Si(100). *J. Electron Spectrosc. Relat. Phenom.* **2004**, 137-140, 85–88.

(46) Virojanadara, C.; Johansson, L. I. Studies of Oxidized Hexagonal SiC Surfaces and the SiC/SiO_2 Interface Using Photoemission and Synchrotron Radiation. *J. Phys.: Condens. Matter* **2004**, 16 (17), S1783–S1814.

(47) Meda, L.; Nicastro, C.; Conte, F.; Cerofolini, G. F. Experimental Valuation of Net Atomic Charge via XPS. *Surf. Interface Anal.* **2000**, 29 (12), 851–855.

(48) Wimmer, M.; Bär, M.; Gerlach, D.; Wilks, R. G.; Scherf, S.; Lupulescu, C.; Ruske, F.; Félix, R.; Hüpkes, J.; Gavrila, G.; Gorgoi, M.; Lips, K.; Eberhardt, W.; Rech, B. Hard X-Ray Photoelectron Spectroscopy Study of the Buried Si/ZnO Thin-Film Solar Cell Interface: Direct Evidence for the Formation of Si–O at the Expense of Zn-O Bonds. *Appl. Phys. Lett.* **2011**, 99 (15), 152104-1–152104-3.

(49) Engstrom, J. R.; Bonser, D. J.; Engel, T. The Reaction of Atomic Oxygen with Si(100) and Si(111): II. Adsorption, Passive Oxidation and the Effect of Coincident Ion Bombardment. *Surf. Sci.* **1992**, 268 (1-3), 238–264.

(50) Ono, Y.; Tabe, M.; Kageshima, H. Scanning-Tunneling-Microscopy Observation of Thermal Oxide Growth on Si(111)7×7 Surfaces. *Phys. Rev. B* **1993**, 48 (19), 14291–14300.

(51) Namiki, A.; Tanimoto, K.; Nakamura, T.; Ohtake, N.; Suzaki, T. XPS Study on the Early Stages of Oxidation of Si(100) by Atomic Oxygen. *Surf. Sci.* **1989**, 222 (2-3), 530–554.

(52) Watanabe, H.; Kato, K.; Uda, T.; Fujita, K.; Ichikawa, M.; Kawamura, T.; Terakura, K. Kinetics of Initial Layer-by-Layer Oxidation of Si(001) Surfaces. *Phys. Rev. Lett.* **1998**, 80 (2), 345–348.

(53) Kageshima, H.; Shiraishi, K. First-Principles Study of Oxide Growth on Si(100) Surfaces and at SiO_2/Si(100) Interfaces. *Phys. Rev. Lett.* **1998**, 81 (26), 5936–5939.

(54) Smirnov, V.; Lambertz, A.; Moll, S.; Bär, M.; Starr, D. E.; Wilks, R. G.; Gorgoi, M.; Heidt, A.; Luysberg, M.; Holländer, B.; Finger, F. Doped Microcrystalline Silicon Oxide Alloys for Silicon-Based Photovoltaics : Optoelectronic Properties , Chemical Composition and Structure Studied by Advanced Characterization Techniques. *Phys. Status Solidi A* **2016**, 1–7.

(55) *For the Si 1s [Si 2s] CL, the given Si^{4+} shift of -4.01 [-3.28] eV equals the difference of the measured Si^{4+} located at 1843.14 [153.67] eV (Figure 1 and S1) and the model obtained bulk binding energy $BE_{Bulk}^{Si\,1s\,[Si\,2s]}$ at 1839.13 [150.39] eV (Table 1, ASA). Si^{1+} is then determined by its relative shift of 2.6 eV to Si^{4+}.*

(56) Kanschat, P.; Mell, H.; Lips, K.; Fuhs, W. Defect and Tail States in Microcrystalline Silicon Investigated by Pulsed ESR. *MRS Online Proc. Libr.* **2000**, 609, A27.3.1–A27.3.6.

(57) Finger, F.; Müller, J.; Malten, C.; Carius, R.; Wagner, H. Electronic Properties of Microcrystalline Silicon Investigated by Electron Spin Resonance and Transport Measurements. *J. Non-Cryst. Solids* **2000**, 266-269, 511–518.

(58) Wieder, S. Amorphous Silicon Solar Cells Comparison of P-I-N and N-I-P Structures with Zinc-Oxide Frontcontact *Ph.D. thesis, Forschungszentrum Jülich* **1999**, 44.

(59) Stuke, J. Problems in the Understanding of Electronic Properties of Amorphous Silicon. *J. Non-Cryst. Solids* **1987**, 97-98, 1–14.

(60) Egelhoff, W. F. Core-Level Binding-Energy Shifts at Surfaces and in Solids. *Surf. Sci. Rep.* **1987**, 6 (6-8), 253–415.

(61) Sze, S. M.; Ng, K. K. Physics of Semiconductor Devices, 3rd ed. *John Wiley & Sons* **2006**.

(62) *The surface-charge density equals the integration of the space-charge density over depth. To compute the number of electrons per surface atom we use that crystalline Si has an atom density of 5×10^{22} cm^{-3},[61] which corresponds to 1×10^{15} cm^{-2}.*

(63) Pieters, B. E.; Stiebig, H.; Zeman, M.; van Swaaij, R. A. C. M. M. Determination of the Mobility Gap of Intrinsic μc-Si:H in P-I-N Solar Cells. *J. Appl. Phys.* **2009**, 105 (4), 044502-1–044502-10.

(64) Pieters, B. E.; Schicho, S.; Stiebig, H. Characterization of the Mobility Gap in μc-Si:H Pin Devices. *MRS Online Proc. Libr.* **2008**, 1066, 1066-A04 - 03–1066-A04 - 08.

(65) Demuth, J.E.; Thompson, W.J.; DiNardo, N.J.; Imbihl, R. Photoemission-Based Photovoltage Probe of Semiconductor Surface and Interface Electronic Structure. *Phys. Rev. Lett.* **1986**, 56 (13), 1408–1411.

(66) Segal, Y.; Ngai, J. H.; Reiner, J. W.; Walker, F. J.; Ahn, C. H. X-Ray Photoemission Studies of the Metal-Insulator Transition in $LaAlO_3/SrTiO_3$ Structures Grown by Molecular Beam Epitaxy. *Phys. Rev. B: Solid State* **2009**, 80 (24), 241107-1–241107-4.

(67) Keski-Rahkonen, O.; Krause, M. O. Total and Partial Atomic-Level Widths*. *At. Data Nucl. Data Tables* **1974**, 14 (2), 139–146.

(68) Krause, M. O.; Oliver, J. H. Natural Widths of Atomic K and L Levels, Kα X-Ray Lines and Several KLL Auger Lines. *J. Phys. Chem. Ref. Data* **1979**, 8 (2), 329–338.

(69) Houben, L.; Luysberg, M.; Hapke, P.; Vetterl, O.; Finger, F.; Carius, R.; Wagner, H. Morphological and Crystallographic Defect Properties of Microcrystalline Silicon: A Comparison between Different Growth Modes. *J. Non-Cryst. Solids* **1998**, 227-230, 896–900.

(70) Jolly, F.; Rochet, F.; Dufour, G.; Grupp, C.; Taleb-Ibrahimi, A. Oxidation of the H-Si(111)-1×1 Surface: High Resolution Si 2p Core-Level Spectroscopy with Synchrotron Radiation. *Surf. Sci.* **2000**, 463 (2), 102–108.

Table of Contents Graphic and Synopsis
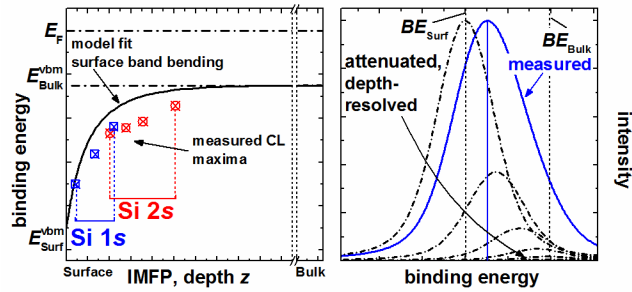
In this article surface oxides and the impact of surface band bending and photoelectron-signal attenuation in silicon thin films on core levels probed with hard X-ray photoelectron spectroscopy (HAXPES) is analyzed. A computational algorithm demonstrates a significant effect on core level shift, line shape, and the band profile estimation. This is especially relevant for these types of studies on surfaces and buried interfaces in semiconductor devices due to the large information depth of HAXPES.

Supporting Information

Pronounced Surface Band Bending of Thin-Film Silicon Revealed by Modeling Core Levels Probed with Hard X-rays

David Wippler*[§], Regan G. Wilks[#⊥], Bart E. Pieters[§], Sacha J. van Albada[&], Dominic Gerlach[#‡], Jürgen Hüpkes*[§], Marcus Bär[#⊥∥] and Uwe Rau[§]

[§]IEK-5 Photovoltaik and [&]Institute of Neuroscience and Medicine Computational and Systems Neuroscience & Institute for Advanced Simulation Theoretical Neuroscience & JARA BRAIN Institute I, Forschungszentrum Jülich GmbH, Wilhelm-Johnen-Straße, D-52425 Jülich, Germany

[#]Renewable Energy, Helmholtz-Zentrum Berlin für Materialien und Energie GmbH, Hahn-Meitner-Platz 1, D-14109 Berlin, Germany

[⊥]Energy Materials In-Situ Laboratory Berlin (EMIL), Helmholtz-Zentrum Berlin für Materialien und Energie GmbH, Albert-Einstein-Str. 15, D-12489 Berlin, Germany

[‡]MANA/Nano-Electronics Materials Unit, National Institute for Materials Science (NIMS), 1-1 Namiki, Tsukuba, Ibaraki 305-0044, Japan

||Institut für Physik und Chemie, Brandenburgische TU Cottbus, Konrad-Wachsmann-Allee 1,

D-03046 Cottbus, Germany

Corresponding Authors: E-mail*: d.wippler@fz-juelich.de.
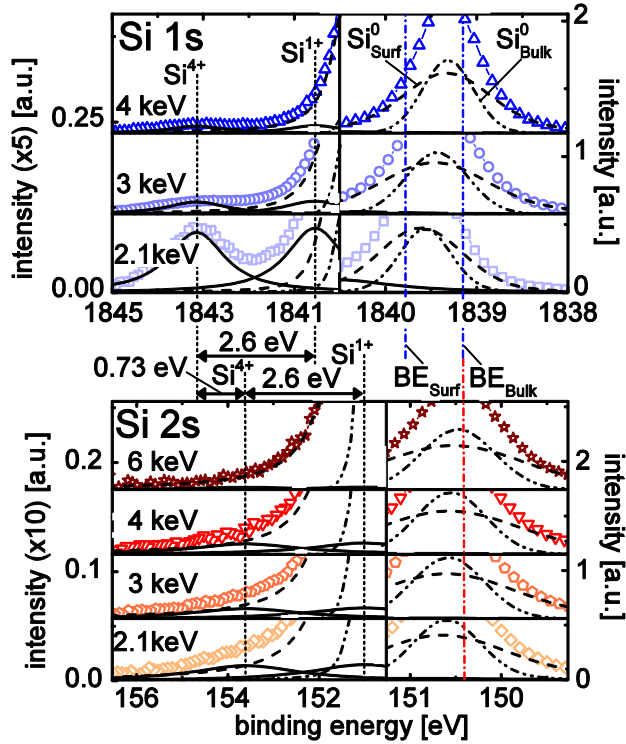
E-mail*: j.huepkes@fz-juelich.de.

Figure S1. Component fits of all measured Si 1s (top) and Si 2s (bottom) spectra of μc-Si:H:B. A linear background is subtracted. The Si-Si feature at lower binding energies (right-hand side) was fitted using two Voigt profiles related to a surface signal weighted component (Si^0_{Surf}) and a bulk signal weighted component (Si^0_{Bulk}). The BE_{Bulk} and BE_{Surf} (only Si 1s) obtained from the computational model are added for comparison. The Si-O_x contribution at higher binding energies (left-hand side, magnified by a factor 5 for Si 1s or 10 for Si 2s) is fitted by one Voigt profile for each Si^{4+} and Si^{1+}. Together with the modeled BE_{Bulk} values the determination of the absolute Si-O_x shift related to Si-Si or between Si 1s and Si 2s becomes possible.

Si-O_x Peak Fit. The oxygen components of the Si 1s and Si 2s CLs were fitted using the procedure described below. It tries to compensate for the rapid drop of the Si-O_x signal intensity with increasing excitation energy as well as for the partial superposition of the Si^{1+} contribution with the dominant Si-Si peak, shown in Figure S1. The left-hand side is adapted to better resolve

the $Si-O_x$ components by increasing the intensity (y-axis) by a factor 5 (Si 1s) or 10 (Si 2s) and by compressing the x-axis in comparison to the right-hand side. The latter is used for the description of the Si-Si peak fit procedure in the next subsection. Note that both left- and right-hand side partly overlap at the cutting line in the x-direction. For the $Si-O_x$ peak fit procedure first a Voigt profile was applied for each $Si-O_x$ signal using the Gaussian width of corresponding Au 4f reference measurements. The Lorentzian width was determined by fitting the 2.1 keV Si^{4+} contribution (strongest intensity) of the Si 1s and Si 2s spectrum, respectively. This Lorentzian widths were then kept fixed and used for the Si^{4+} contribution of all other spectra measured with different excitation energies as well as for all Si^{1+} peaks, resulting in an equal shape of Si^{4+} and Si^{1+} for each excitation energy for a given CL. This is based on the assumption of the same chemical environment for Si^{1+} and Si^{4+} as described in the main article. The 2.1 keV Si 1s spectrum was also used to extract the Si^{4+}/Si^{1+} intensity ratio and their relative binding energy shift of 2.6 eV. This intensity ratio and energy shift were then held constant to fit the Si^{1+} component in the experimental data for all other excitation energies including the Si 2s spectra, whereas the Si^{4+} peak position and intensity remained free fitting parameters.

Si-Si Peak Fit. PES measurements consist of signals from all depths z with decreasing intensity according to the photoelectron-signal attenuation. For CL lines these measured signals are usually described using a Voigt profile with the Lorentzian as the lifetime broadening and the Gaussian as the system response function. This CL line description may be a suitable approximation for very thin layers (see section 'Si-O_x peak fit' above), highly surface-sensitive measurements, or in case of flat-band conditions (i.e., no surface band bending). In the presence of a pronounced surface band bending, however, the depth-resolved attenuated signals are shifted towards each other and affect the measured signal of layers thicker than a monolayer. This is the

case for the measured Si-Si feature of our Si 1s and Si 2s CL spectra. The measured total signal

becomes asymmetric and can be approximated by a fit with a large number of Voigt profiles

each of which contributes with four parameters to the fitting procedure. Using a large number of

profiles may result in a good fit, but the parameters are poorly constrained without further

assumptions. Thus we limited the fit to two Voigt profiles for the main Si-Si peak to account for

its asymmetry, as shown in Figure 2a of the main article. Even with only two Voigt profiles,

further constraints are required. The shift of the peak that account for the asymmetry cannot

exceed the band bending at the surface eV_{bb}. We here defined a fit for which the area ratio of the

two Si-Si Voigt profiles equals the intensity ratio of all signals from depth $z <$ IMFP (Si^0_{Surf}) to

all signals from depth $z >$ IMFP (Si^0_{Bulk}). Si^0_{Surf} is broadened and slightly shifted to higher

binding energies compared to Si^0_{Bulk} due to the stronger impact of CADDS (convolution of

attenuated depth-dependent signals) on signals from $z <$ IMFP. Both contributions shift with

increasing IMFP to lower binding energies due to an increase of bulk signal for Si^0_{Surf} and a

decrease of surface signal for Si^0_{Bulk} while their relative energetic positions slightly converge (see

Figure S1, right-hand side). Note that Si^0_{Surf} and Si^0_{Bulk} do not represent the real surface or bulk

CL position because those positions are not accessible from a simple fit to measured data,

independent from the chosen excitation energy or IMFP. This is clearly visible by comparing

their energetic positions with the "real" CL positions BE_{Surf} and BE_{Bulk} obtained from the

model, which are indicated by vertical dash-dotted lines in Figure S1a, right-hand side.
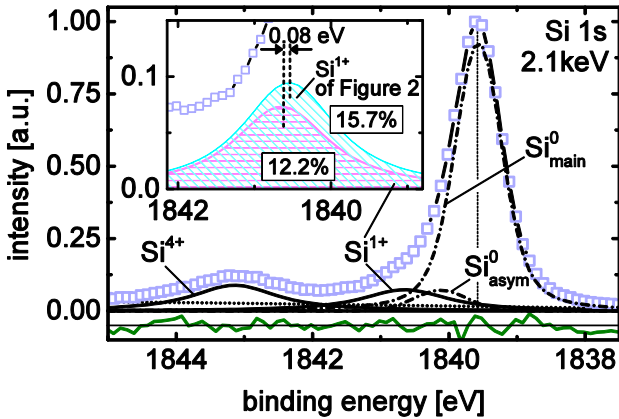
Figure S2. Alternative fit for the Si-Si components (Si_{main}^{0} and Si_{asym}^{0}) in comparison to Figure 2a (main article) and its influence on the Si^{1+} oxygen contribution (inset). Here, the Si-Si feature is fitted by a dominant Voigt profile Si_{main}^{0} with a smaller, but more strongly shifted Voigt profile Si_{asym}^{0} to account for asymmetry. The residual (at the bottom, multiplied by a factor 3) indicates an inferior fit of the Si-Si feature compared to the one used in Figure 2a. In the inset, the magenta horizontally hatched area represents the related Si^{1+} signal, while the cyan diagonally hatched area shows the corresponding Si^{1+} signal of the fit depicted in Figure 2a. Their relative shift and their integrated intensity (in % of the combined integrated intensity of Si-O_x and Si-Si) are indicated. In general, the used Si-Si fit procedure has only a minor influence on the results of the model best fit.

An alternative Si-Si two-component Voigt fit is shown in Figure S2 for comparison, for which the main contribution of the signal is fitted by one Voigt profile (Si_{main}^{0}) and only a small contribution remains for the peak that account for the asymmetry (Si_{asym}^{0}). In this case, the shift of around 0.6 eV between both Si-Si Voigt profiles nearly reaches the extent of the band bending at the surface. The fit residuals (multiplied by a factor 3) are indicated below Figures 2a and S2 for comparison. While for the high binding energy region dominated by the Si-O_x contribution

both fit residuals are equal, the fit of the Si-Si contribution at the right-hand side in Figure S2 deviates stronger from the measured data compared to the one shown in Figure 2a. Depending on the type of Si-Si fit also the intensity and position of the Si^{1+} peak are slightly affected (see inset in Figure S2). However, the results of the applied model fit are largely independent of the choice of fit for the main Si-Si peak. Even directly model fitting the measured data without subtraction of the oxygen contribution or linear background led to model best fit values within the +10% error ranges of the model best fit presented in this publication. In that case the natural Lorentzian widths and the band bending at the surface became slightly larger while the bulk CL positions remained nearly unchanged (not shown). This is understandable, as the computational model that only accounts for CADDS and not for the $Si-O_x$ contribution tries to compensate the presumed Si-Si high-binding energy shoulder formed by the Si^{1+} signal, while the Si^{4+} signal has no impact due to its larger energetic distance.

Direct Surface Band Bending Estimation. The DA and ASA model best fit allow the determination of the offset between the Si 1s and Si 2s CL maxima. However, without modelling a band profile it is difficult to find an appropriate alignment of the Si 1s and Si 2s CLs to make use of the full information depth range. As solution we used the similar IMFP of the 4 keV Si 1s (~4.42 nm, upright triangle) and the 2.1 keV Si 2s (~4.07 nm, diamond) data (see Figure 3a) to align the positions of our Si 1s and Si 2s measurements to each other. Together with the surface and bulk sensitivity of the 2.1 keV Si 1s (square) and 6 keV Si 2s (star) measurements we estimated the surface band bending in the direct case as sum of the measured CL shifts for Si 1s of (-0.26 ± 0.05) eV and Si 2s of (-0.13 ± 0.05) eV. The parabolic extrapolation considers the fact, that the most surface-sensitive Si 1s peak (IMFP ~ 0.90 nm) still does not represent the CL binding energy at the very surface. The value of $eV_{bb} = (-0.45 \pm 0.03)$ eV with a depletion region

of about 9.9 nm was obtained by aligning the measured data according to the description above and parabolic extrapolation of the measured data to the surface.

Inverse Modeling. The determination of a band profile for a given sample requires the algorithm to fit measured CL lines. The treatment of this inverse problem results in a large number of possible solutions that can only be restricted through careful selection of the model parameters and their ranges.

Band profile parameters – In our case, the main restriction of possible solutions is given by the knowledge of the typical band profile that causes the shift. This leads to a major simplification compared to models dealing with, e.g., chemical distributions that are generally unknown.[1] In ASA[2] the most important parameters to model the band profile are given by the band bending at the silicon surface eV_{bb} and the density of dangling bonds n_{db}, respectively. Furthermore, ASA requires the band gap E_{Gap} and the bulk position of the Fermi level E_F for more precise calculations. The latter value has been determined to 0.25 eV above the bulk valence band maximum.[3] E_{Gap} was assumed to be 1.25 eV.[4,5] The direction of the measured CL binding energy shift indicates a downward surface band bending. Due to the high density of states in the conduction band it is to be expected that the Fermi level lies between the conduction band minimum and E_F of the bulk.[6] Thus we specify a range of eV_{bb}: [-1, 0] eV under the assumption that the band gap at the surface is identical to the bulk. The density of dangling bonds n_{db} is not exactly known and therefore was varied in a wide range: $[10^{17}, 10^{21}]$ cm^{-3}. For DA modeled band profiles, the band bending at the silicon surface eV_{bb} and its range remain as a parameter, but n_{db} must be replaced by the depletion region width w_{dr}. Its limits can easily be identified as the thickness of the investigated layer, in our case μc-Si:H:B: [0, 38.5] nm.

Bulk CL binding energy – The next parameters to consider are the bulk CL binding energies $BE_{Bulk}^{Si\ 1s}$ and $BE_{Bulk}^{Si\ 2s}$. They cannot generally be taken directly from measurements, because the measured peaks are affected by CADDS. The modeled BE_{Bulk} is set to 0 eV, resulting in an offset between the modeled peak positions and the measured ones. We thus estimate $BE_{Bulk}^{Si\ 1s}$ and $BE_{Bulk}^{Si\ 2s}$ by shifting the modeled CL peaks to obtain the best fit between model and experiment. Note that we always shift all 1s CL lines with one *value* for $BE_{Bulk}^{Si\ 1s}$, and work likewise for the 2s CL lines. Reported binding energies for Si 1s and Si 2s vary in literature and were used as reasonable BE_{Bulk} parameter ranges with $BE_{Bulk}^{Si\ 1s}$: [1838.0, 1839.4] eV, $BE_{Bulk}^{Si\ 2s}$: [150, 151] eV.[7]

Natural Lorentzian line width – The shape of the modeled Voigt profile can be modified by varying the Gaussian $fwhm_\sigma$ and the natural Lorentzian $fwhm_\Gamma$. There are two Voigt profiles to consider, the Si 1s and Si 2s profile, doubling the number of additional parameters to four. Fortunately, we are able to identify the machine-related Gaussian width from Au 4f reference measurements for each excitation energy. It is determined for the measurement system and independent of the specimen. The lifetime broadening $fwhm_\Gamma$ of the Au $4f_{7/2}$ lines was in accordance with literature and considered in the determination of the Gaussian $fwhm_\sigma$.[8,9] The resulting $fwhm_\sigma$ are listed in Table 2. The range of the natural $fwhm_\Gamma$ of Si was then estimated by using the Lorentzian width of the measured signal $fwhm_{\Gamma\ St}{}^{*e}$ as the upper bound, because $fwhm_{\Gamma\ Sz}$ of the initial signal S_z (which we consider to be the natural $fwhm_\Gamma$) must be smaller. The lower bound of the initial Lorentzian width was selected in a way ensuring that the Lorentzian width of the modeled integrated signal $fwhm_{\Gamma\ St}{}^{*m}$ was smaller than its respective value for the measured signals $fwhm_{\Gamma\ St}{}^{*e}$, which results in the following range for $fwhm_\Gamma^{Si\ 1s}$: [200, 1000] meV and $fwhm_\Gamma^{Si\ 2s}$: [200, 1200] meV.[10]

These considerations finally lead to a 6-dimensional bounded parameter space. Table S1

summarizes the model parameters and their respective ranges.

Table S1. Model parameters and ranges

Parameters	range	limitation
eV_{bb} [eV]	[-1, 0]	see text, literature[6]
n_{db} [10^{20} cm^{-3}] (only ASA)	[0.001, 10]	literature[4]
w_{dr} [nm] (only DA)	[0, 38.5]	sample thickness[11]
$BE_{Bulk}^{Si\,1s}$ [eV]	[1838.0, 1839.4]	literature[7]
$BE_{Bulk}^{Si\,2s}$ [eV]	[150, 151]	literature[7]
$fwhm_{\Gamma}^{Si\,1s}$ [meV]	[200, 1000]]	width of S_t^{*e} for Si 1s[10]
$fwhm_{\Gamma}^{Si\,2s}$ [meV]	[200, 1200]	width of S_t^{*e} for Si 2s[10]

Parameters and ranges chosen for the minimization routine to model fit experimental Si 1s and Si 2s CL lines for μc-Si:H:B

Minimization Routine for the Inverse Problem. The 6-dimensional parameter space required

an efficient global optimizer to find the best fit of the modeled Si 1s and Si 2s CL lines to the

measured peaks with reasonable calculation time. The experimental data were prepared by

deducting a linear background and the observed Si-O$_x$ contributions (see main article). In order

to ensure a good signal-to-noise ratio, only data points of the measured Si-Si peaks in an interval

down to 5% of the peak maximum were used to determine the root-mean-square deviation

(RMSD) for each peak. The total error of the model fit is then calculated as the averaged RMSD

of all peaks. A step size of 0.1 eV and a range of about 2 eV (Si 1s) and 3 eV (Si 2s) were

therefore considered for each peak. The main contribution to RMSD is given by the range of the

high peak intensities. Thus the influence of specific assumptions, like the subtraction of a

background or oxygen contribution is suppressed. We tested different assumptions and the

resulting values were still within the +10% error ranges of the assumptions used in the main article listed in Table 1.

In a first step, a genetic algorithm was used.[12,13] It generates a random population of solution vectors within the limited regime of the parameter space and calculates the averaged RMSD for each given vector. The next population is generated in the vicinity of its predecessor with smallest averaged RMSD. A fraction of this population, called mutation rate, is chosen to be distributed randomly to avoid being trapped in a local minimum. For our problem we found good results for a population size of 200, 100 iterations and a mutation rate of 25%. We used four different random number sets of starting vectors for the genetic algorithm, which finally result in four different solution vectors located in a very small area around the presumed absolute minimum. In a second step these slightly different solution vectors of the genetic algorithm were used as the starting points for Matlab´s local minimizer "fminsearch",[14] which uses the Nelder-Mead downhill simplex algorithm.[15] All four starting points resulted in the same final solution vector with minimal averaged RMSD that was finally used for the model best fit. fminsearch was also used to estimate the error value for each model parameter, as described next.

Parameter Error Estimation. To estimate the error value for each model parameter, we ran the minimization routine as described above but forced the parameter under consideration to remain at a specific value. By varying this value stepwise within the limiting range of the parameter and applying this procedure to all model parameters, we obtained an approximation to the surface of local minima, i.e., the minimum width of the optimum along the direction of one parameter axis in parameter space. Figure S3 shows the results for the different parameters (ASA: magenta solid lines, DA: blue dashed lines). The points indicate each chosen fixed parameter value for which the minimization routine was applied, and the absolute minimum for each parameter is indicated

by a thick vertical solid line. The width of the optimum is a measure for the uncertainty in the determined parameter values. We determine the width as the interval around the optimum which starts and ends at an error 10% higher than the optimum, the +10% range (region between thin vertical solid lines).
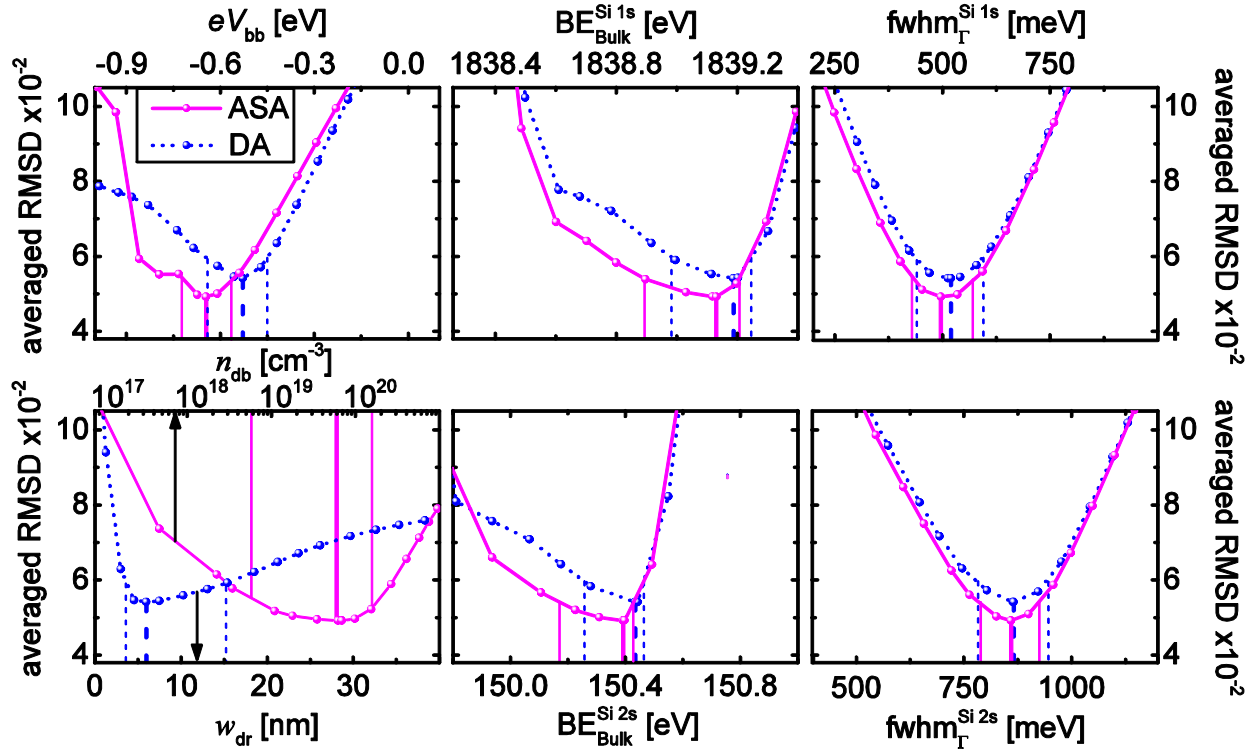

Figure S3. Averaged RMSD as a function of model parameters for ASA (magenta) and the depletion approximation (DA, blue). The points indicate fixed parameter positions for which the minimization routine was applied, the connecting lines are guides to the eye. The vertical thick solid (ASA) or dashed (DA) lines indicate the absolute minimum of the respective parameter. Its +10% range lies between vertical thin solid (ASA) or dashed (DA) lines.

REFERENCES

(1)   Cumpson, P. J. Angle-Resolved XPS and AES: Depth-Resolution Limits and a General Comparison of Properties of Depth-Profile Reconstruction Methods. *J. Electron Spectrosc. Relat. Phenom.* **1995**, 73 (1), 25–52.

(2)   ASA. ASA, Advanced Semiconductor Analysis, Version 5.30 degrading since 2012 (compiled on Feb 4 2013), © 1993/2013 Lab of ECIM / DIMES Delft University of Technology.

(3)   Gerlach, D.; Wilks, R. G.; Wippler, D.; Wimmer, M.; Lozac'h, M.; Félix, R.; Mück, A.; Meier, M.; Ueda, S.; Yoshikawa, H.; Gorgoi, M.; Lips, K.; Rech, B.; Sumiya, M.; Hüpkes, J.; Kobayashi, K.; Bär, M. The Silicon/Zinc Oxide Interface in Amorphous Silicon-Based Thin-Film Solar Cells: Understanding an Empirically Optimized Contact. *Appl. Phys. Lett.* **2013**, 103 (2), 023903-1–023903-5.

(4)   Pieters, B. E.; Stiebig, H.; Zeman, M.; van Swaaij, R. A. C. M. M. Determination of the Mobility Gap of Intrinsic μc-Si:H in P-I-N Solar Cells. *J. Appl. Phys.* **2009**, 105 (4), 044502-1–044502-10.

(5)   Pieters, B. E.; Schicho, S.; Stiebig, H. Characterization of the Mobility Gap in μc-Si:H Pin Devices. *MRS Online Proc. Libr.* **2008**, 1066, 1066-A04 - 03–1066-A04 - 08.

(6)   Sze, S. M.; Ng, K. K. Physics of Semiconductor Devices, 3rd ed. *John Wiley & Sons* **2006**.

(7)   NIST   XPS   Database.   *NIST   XPS   Database;* *http://srdata.nist.gov/xps/EngElmSrchQuery.aspx?EType=PE&CSOpt=Retri_ex_dat&Elm=Si.*

(8)   Citrin, P. H.; Wertheim, G. K.; Baer, Y. Core-Level Binding Energy and Density of States from the Surface Atoms of Gold. *Phys. Rev. Lett.* **1978**, 41 (20), 1425–1428.

(9)   Aksela, S.; Kantia, T.; Patanen, M.; Mäkinen, A.; Urpelainen, S.; Aksela, H. Accurate Free Atom–Solid Binding Energy Shifts for Au and Ag. *J. Electron Spectrosc. Relat. Phenom.* **2012**, 185 (8-9), 273–277.

(10) Keski-Rahkonen, O.; Krause, M. O. Total and Partial Atomic-Level Widths*. *At. Data Nucl. Data Tables* **1974**, 14 (2), 139–146.

(11) Gerlach, D.; Wippler, D.; Wilks, R. G.; Wimmer, M.; Lozac´h, M.; Félix, R.; Ueda, S.; Yoshikawa, H.; Lips, K.; Rech, B.; Sumiya, M.; Kobayashi, K.; Gorgoi, M.; Hüpkes, J.; Bär, M. P-Type a-Si:H/ZnO:Al and μc-Si:H/ZnO:Al Thin-Film Solar Cell Structures — A Comparative Hard X-Ray Photoelectron Spectroscopy Study. *IEEE Photovoltaic Spec. Conf. , 38th* **2013**, 2, 1–5.

(12) Haupt, R. L.; Haupt, S. E. Practical Genetic Algorithms *John Wiley & Sons* **2004**.

(13) Krumscheid, S. Optimizing the Interconnection Geometry of Thin-Film Solar Modules Using the Finite Element Method *Master's thesis, Aachen University of Applied Science* **2010**.

(14) MATLAB Version 8.0.0.783 (R2012b), Copyright 1984-2012. The MathWorks, Inc. Protected by U.S. and international patents. See www.mathworks.com/patents. MATLAB and Simulink   are   registered   trademarks   of   The   MathWorks,   Inc.   See www.mathworks.com/trademarks.

(15) Nelder, J. A.; Mead, R. A Simplex Method for Function Minimization. *The Computer Journal* **1965**, *7* (4), 308–313.